SCIENTIFIC REPORTS

OPEN

SUBJECT AREAS:
ATMOSPHERIC SCIENCE
ENVIRONMENTAL SCIENCES

Received
20 March 2014

Accepted
9 June 2014

Published
1 July 2014

Correspondence and requests for materials should be addressed to R.K.C. (rajan.chakrabarty@gmail.com)

Soot superaggregates from flaming wildfires and their direct radiative forcing

Rajan K. Chakrabarty[1,2], Nicholas D. Beres[2], Hans Moosmüller[2], Swarup China[3], Claudio Mazzoleni[3], Manvendra K. Dubey[4], Li Liu[5] & Michael I. Mishchenko[5]

[1]Department of Energy, Environmental & Chemical Engineering, Washington University in St. Louis, St. Louis, MO 63130, USA, [2]Desert Research Institute, Nevada System of Higher Education, Reno, Nevada, USA, [3]Atmospheric Sciences Program, Michigan Technological University, Houghton, Michigan, USA, [4]Earth System Observations, Los Alamos National Laboratory, Los Alamos, New Mexico, USA, [5]NASA Goddard Institute for Space Studies, New York, NY 10025, USA.

Wildfires contribute significantly to global soot emissions, yet their aerosol formation mechanisms and resulting particle properties are poorly understood and parameterized in climate models. The conventional view holds that soot is formed via the cluster-dilute aggregation mechanism in wildfires and emitted as aggregates with fractal dimension $D_f \approx 1.8$ mobility diameter $D_m \leq 1$ μm, and aerodynamic diameter $D_a \leq 300$ nm. Here we report the ubiquitous presence of soot superaggregates (SAs) in the outflow from a major wildfire in India. SAs are porous, low-density aggregates of cluster-dilute aggregates with characteristic $D_f \approx 2.6$, $D_m > 1$ μm, and $D_a \leq 300$ nm that form via the cluster-dense aggregation mechanism. We present additional observations of soot SAs in wildfire smoke-laden air masses over Northern California, New Mexico, and Mexico City. We estimate that SAs contribute, per unit optical depth, up to 35% less atmospheric warming than freshly-emitted ($D_f \approx 1.8$) aggregates, and ≈90% more warming than the volume-equivalent spherical soot particles simulated in climate models.

On a global scale, wildfires emit approximately 34% of total atmospheric soot mass, while in certain regions such as southeast Asia and Russia, these fires contribute as much as 63% of regional soot mass emissions[1]. In the context of climate change, soot emitted from wildfires and biomass burning episodes contribute to one of the largest uncertainties in current estimates of radiative forcing[2]. This large uncertainty is due to poor understanding of the microphysical properties of wildfire-emitted soot and their parameterizations in models and satellite retrieval algorithms[2,3]. In recent years, researchers have made thorough efforts to characterize these properties for soot emitted from small-scale, controlled combustion systems—such as prescribed and slash burns—as a function of various process parameters such as fuel type, flame temperature, environmental conditions driving the combustion process, and interrelationships of these parameters[4–7]. These studies have been conducted under the assumption that they may closely mimic natural wildfires in their soot formation mechanism and emitted particle properties.

Soot formation in small-scale combustion systems takes place in the cluster-dilute aggregation regime, wherein average aggregate–aggregate separation in the aerosol system is much larger than aggregate size[8]. Aggregation in this regime proceeds via a three-dimensional, diffusion-limited growth mechanism, governed by the mean-field Smoluchowski equation[8,9]. The resultant morphology of aggregates emitted into the atmosphere from this regime is described by a fractal dimension $D_f \approx 1.8$, maximum lengths up to 1 μm, mobility diameter $D_m < 1$ μm, and aerodynamic diameter D_a—used for estimating the probability of deposition within lungs[10]—less than 300 nm[5]. These aggregates consist of tens to a few hundred monomers, with each monomer typically 30–50 nm in diameter[5]. Through atmospheric processing, it is possible for these aggregates to collapse into sphere-like morphologies with $D_f \approx 2.6$[11,12]. Climate modelers assume the morphology of bare soot aggregates to be spherical in model parameterizations[2,13].

The unpredictable occurrence and nature of large-scale wildfires severely limit the opportunity for in-plume sampling of smoke particles for analysis of particle properties and understanding of soot formation mechanisms[3,4]. Single-particle electron microscopy analysis provides crucial information toward accurate and size-unconstrained characterization of aerosol microphysical properties[5,14]. Additionally, information on the aerosol formation mechanism can be deduced from single-particle electron micrographs[8,9,15,16]. There have been only a limited number of studies conducted to investigate aerosols emitted from natural wildfires using electron microscopy[17–23]. The majority of these studies sampled particles during a fire's smoldering combustion phase (low-

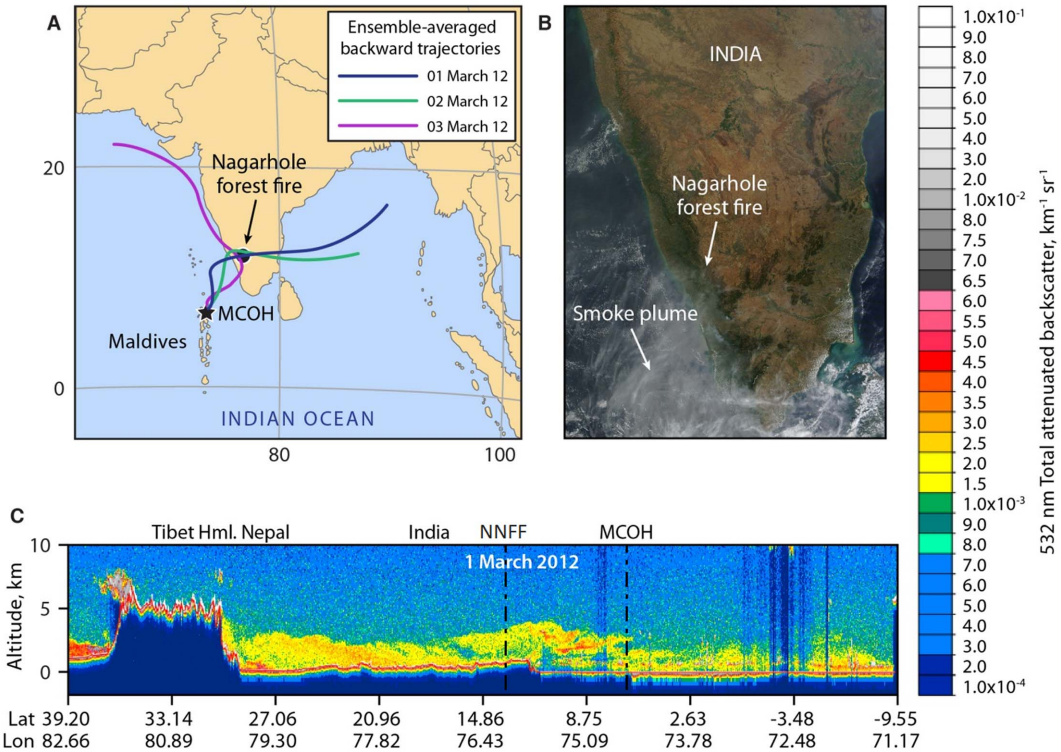

Figure 1 | The 2012 Nagarhole forest wildfire smoke plume transport. (A) Average of NOAA HYSPLIT ensemble trajectories ending at the Maldives Climate Observatory–Hanimaadhoo, Maldives (MCOH) on 01, 02, and 03 March 2012. (*Image created using Adobe Photoshop™*); (B) Visible imagery of the Indian Peninsula from the MODIS sensor aboard the Terra satellite for 28 February 2012. (*Image obtained from NASA Near Real-time (NRT) data archive*); (C) 532 nm backscatter return signal from the CALIOP Lidar aboard the CALIPSO satellite showing vertical distribution of aerosols (*Image obtained from NASA CALIPSO data archive*). The color scale on the right indicates the strength of the LIDAR return signal: boundary layer clouds usually show up as grey or white; cirrus clouds range from yellow to grey; and aerosols show up as green, yellow, and red (indicating low, medium, and high loadings, respectively).

temperature). Exceptions have been the aircraft sampling studies conducted during the 1990's in the over-fire regions of flaming forest fires in Brazil and southern Africa[17,18]. Observations of unusually large soot aggregates were made from these fires, but the investigators failed to distinguish the microphysical properties of these particles from conventional sub-micron soot aggregates. As a result, these unique observations have gone unnoticed, and there has been no follow-up investigation conducted on the formation mechanism and frequency of occurrence of these unusually large soot aggregates, their microphysical properties, and their potential impact on radiative forcing and health.

Here, we investigate particles contained in the flaming-phase plumes of the Nagarhole National Forest fire (NNFF)[24] in Karnataka (India) and find the ubiquitous occurrence of superaggregates (SAs), a hitherto unrecognized form of soot distinct from conventional sub-micron aggregates. We report additional observation of these SAs in wildfire smoke-laden air masses over Sacramento (Northern California, USA), Los Alamos (New Mexico, USA), and the Mexico City metropolitan area (Mexico), respectively. Based on the unique morphological properties of SAs, we discuss their possible formation mechanism and their potential impact on human health. We also compute numerically-exact optical properties of these particles and compare them with those of sub-micron size soot particles. We make use of the optical properties to calculate direct radiative forcing efficiencies of SAs at the top of the atmosphere and discuss their net warming or cooling of the atmosphere. Finally, we address the need for future research to better understand and characterize the detection and atmospheric processing of soot SAs for quantitatively estimating their impact on climate and health.

Results

We collected aerosol samples for scanning electron microscopy (SEM) analysis downwind of the NNFF over the Indian Ocean at the Maldives Climate Observatory on Hanimaadhoo Island (MCOH) (6.78° N, 73.18° E). The NNFF, which lasted for a week beginning February 27, 2012, burned approximately 35 km^2 of dry deciduous forest containing dry bamboo and teak trees. Dense smoke from intense flaming combustion was reported, with the event turning into a firestorm within a day[24]. The MCOH aerosol number concentration increased from about 800 to 3000 cm^{-3} during this period. The months of November through May constitute the dry season in South Asia, when low-level flow brings a polluted air mass from Asia to the Indian Ocean[25]. Ensemble back-trajectory analyses (Fig. 1a; Fig. S1 in supplementary information) coupled with satellite imagery and the Cloud Aerosol Lidar and Infrared Pathfinder Satellite (CALIPSO) measurements (Fig. 1 b and c) show a low-level polluted air mass—between 1 to 3 km above sea level—transported from the forest fire site flowing southwest over the Indian Ocean. Gas chromatography interfaced with mass spectrometry analyses of aerosol samples, revealed the presence of levoglucosan—a molecular marker for biomass burning emissions[26]—in trace amounts (about 0.09 ng/m^3).

To investigate how commonly these SAs occur in different geographical locations and atmospheric conditions, we sampled aerosols contained in wildfire smoke-laden air masses over Sacramento during the CARES (Carbonaceous Aerosol and Radiative Effects Study)[27] in June 2010 and over Mexico City as part of the MILAGRO (Megacity Initiative: Local And Global Research Observations)[28,29] study during March-June 2006. Finally, in 2011 at Los Alamos, we sampled the downwind plumes of the Las Conchas wildfire[19], the second largest wildfire in the state's history.

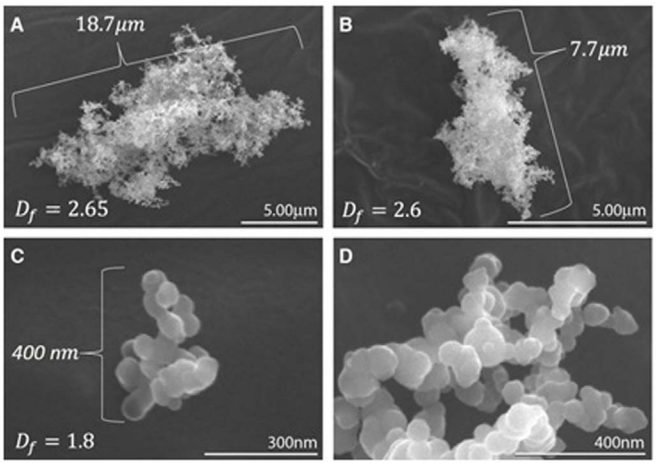

Figure 2 | Soot superaggregate morphology and particle formation mechanism in wildfires. (A, B) SEM images of typical soot SAs observed from sampling of smoke plumes from the Nagarhole forest fire. These aggregates were greater than 5 microns in maximum length, made of thousands of 45–50 nm diameter carbon monomers, and had a characteristic cluster-dense fractal dimension $D_f \approx 2.6$. (C) A typical sub-micrometer size aggregate, made of a few tens of monomers, with a characteristic cluster-dilute $D_f \approx 1.8$. (D) Magnified micrograph of a soot SA from this study, highlighting the low degree of organic carbon coating between monomers and showing no visible evidence of atmospheric processing during long-range transport.

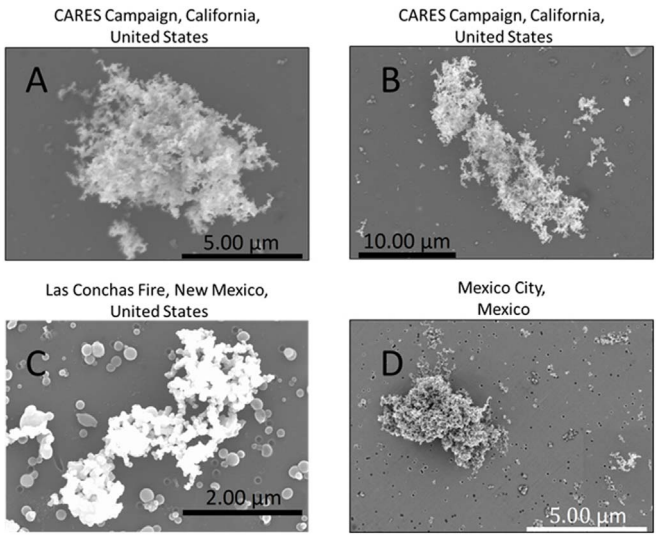

Figure 3 | Soot superaggregates observed in biomass burning plumes in different locations in USA and Mexico. (A, B) Typical soot SAs observed in the Sacramento urban area. The sampled air mass containing biomass burning smoke particles is believed to be transported from the neighboring Sierra Nevada foothills and San Joaquin County[27,57] (C) The Las Conchas fire was the second largest wildfire in the state history of New Mexico burning an area of 634 km^2. The sampled smoke plumes from this fire for this study were mostly from smoldering phase mixed with intermittent flaming phase. As a result, we observed majority (≈80%) of particles to be spherical tar balls, observable in the background of the soot SA particle[19]. (D) A soot SA sampled in Mexico City. The air mass containing these particles is believed to originate from burning of pine savannas in the mountains near Mexico City[28].

Morphological properties of soot superaggregates. We measured the structural and fractal properties of individual carbonaceous particles collected from smoke plumes over the four locations using established image analysis routines[5]. The fractal properties of individual particles were quantified using the perimeter and ensemble methods[30–32]. Electron micrographs of typical SAs observed at the four sampling sites are shown in Fig. 2 and 3. The SAs consisted of aggregates of sub-micrometer size, cluster-dilute soot aggregates with characteristic $D_f = 1.9 \pm 0.2$ (Fig. 2c). The mean maximum length scales of SAs were between 10 and 20 μm, and SAs had distinct $D_f = 2.6 \pm 0.1$.

Our analysis showed that a typical SA consisted of around 3000 monomers, after accounting for apparent monomer overlap, which is parameterized by a power-law factor 1.09[33]. Observation of $D_f = 1.9$ sub-micron aggregates within individual SAs confirms that the SAs were formed via percolation of these aggregates in the fires. High magnification images (Fig. 2d) of NNFF revealed minimal coating of condensed organic matter on the monomers. This suggested that these particles were formed under near unity net equivalence ratio[34] and resisted atmospheric processing during long-range transport[11]. Alternatively, it could be that there was not enough condensable organic matter available in the flaming fire plumes of NNFF (see table S1 in supplementary information) to coat the SAs.

We analyzed 69 individual carbonaceous particles collected on SEM filters from the NNFF. Approximately 99% and 75% of the particle mass and number, respectively, were soot SAs[9,31,32,35], with the remaining being aggregates (Fig. 4). We probed the elemental composition of the particles using energy dispersive X-ray spectroscopy (EDX), finding carbon and oxygen to be their primary constituents. No tar balls[22,36] or particles with inorganic inclusions were observed. We analyzed 580 particles from the CARES campaign and found approximately 16% of the total aerosol particle number was SAs. The remaining 57% and 27% of particles were externally sub-micron soot (occurring as bare and mixed with organic carbon) and dust particles, respectively. The SAs observed in samples from MILAGRO and the Las Conchas fires were less than 1% in number. Aerosol types in these two locations were mostly organic carbon and tar balls[19,20,28,29,37], suggesting dominant emission from the smoldering phase of wildfires.

For the SAs and cluster-dilute aggregates observed at MCOH and during CARES, we calculated their mobility diameters D_m[14,38] and mass distributions (Fig. 4 and 5) based on their single-particle projected area equivalent diameters[14]. The SAs had a range of D_m between 1 and 20 μm with a mean $D_m \approx 3$ μm. The monomer number size distribution could be described by a mono-modal log-normal size distribution with a mean monomer diameter of 50 nm and a standard deviation of 5 nm. We observed a majority (95%) of SAs in the third stage, $D_a < 0.3$ μm, of the impactor used for aerosol collection. Although characterized by very large geometric diameters (D_m), the low D_a of SAs suggest that they are highly porous, have low effective densities, and could get deposited in the innermost lung airways and alveoli via the process of diffusion deposition, similar to soot aggregates[10,39]. However, the extent of lung penetration of SAs depends on particle D_a[40]. Super-micron size porous carbon aggregates, similar to soot SAs in this study, have been synthesized in the laboratory[41], and were observed to have effective particle densities as low as 2.5 mg/cm^3.

Discussion

Superaggregate formation mechanism. SAs are formed when cluster-dilute aggregates enter into a cluster-dense aggregation regime in flames[35]. This regime, defined by a small ratio of the mean aggregate nearest-neighbor separation to aggregate size and by enhanced kinetics, results in the aggregates sticking together and percolating to form a volume spanning SA with a universal $D_f \approx 2.6$[9,35]. SAs usually consist of more than a few thousand monomers and are greater than 1 μm in length[31,32]. Over small length scales, SAs have a $D_f \approx 1.8$ because of their formation via percolation of cluster–dilute aggregates[9].

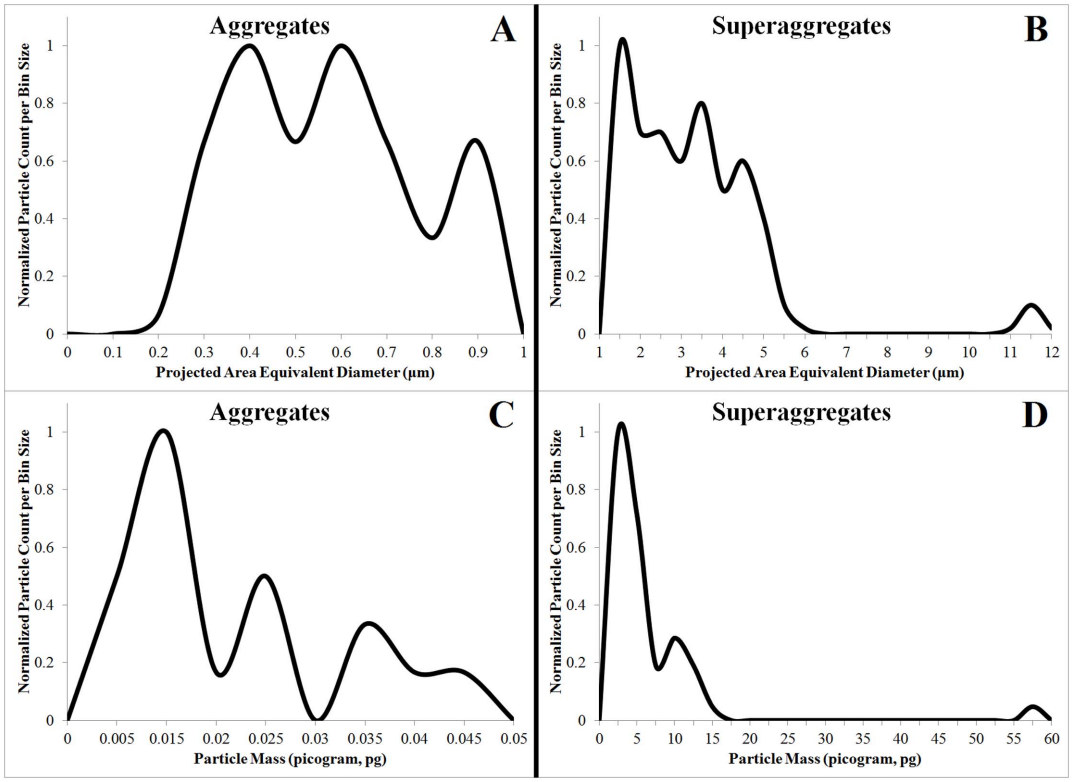

Figure 4 | Number distribution of soot aggregates and superaggregates from the Nagarhole forest fire. (A, B) Number size distribution of the particles is calculated in terms of the projected area equivalent diameter, which is equivalent to particle mobility diameter. (C, D) Single particle mass distribution, calculated from two-dimensional particle images using a carbon monomer density value = 1.8 g/cm^3. It is to be noted that sea-salt particles from the Indian Ocean accompanied the carbonaceous aerosols and were excluded from this analysis.

With the exception of large-scale sooty and turbulent fires[32], upward-rising flame systems cannot emit SAs into the atmosphere due to their narrowing flame fronts and associated buoyancy-driven aggregate fragmentation effects[31]. For SAs to be emitted as final products, an aggregating system must maintain the right physical conditions in terms of threshold particle volume fractions and residence time. A large-scale turbulent flame system provides these conditions by trapping sub-micron aggregates in its vortices[9,31,32,42] (Fig. 6). Once trapped, these aggregates begin to jam together under high particle volume fraction conditions to form SAs. For the soot SAs observed in this study, we hypothesize that they were formed in the vortices of the wildfire flame bodies and subsequently emitted to the atmosphere.

Impact on direct radiative forcing. Quantitative knowledge of the soot morphologies enabled numerically-exact superposition *T*-matrix modeling of single-particle optical properties—asymmetry parameter g and single scattering albedo ω—at 550 nm as functions of aggregate D_f and monomer number (Fig. 7a and b). We also computed these parameters using Mie theory for volume-equivalent spherical particles[14] as used by current climate models. Aggregate simulations and their *T*-matrix modeling methods are described in detail elsewhere[43]. Note that the *T*-matrix calculations required significant computational power and time, limiting the total number of monomers that could be investigated to 1000, but it is likely that these results are broadly representative of SA optical properties. Both g and ω are fundamental parameters for aerosol radiative transfer calculations[44]. ω is the ratio of particle scattering to extinction cross section, and ranges between 0 for a purely absorbing particle to +1 for a purely scattering particle. The asymmetry parameter (g) is defined as the intensity-weighted average cosine of the scattering and ranges between −1 for entirely backscattered light to +1 for entirely forward scattered light. ω increases with increasing monomer number as well as with D_f in both the aggregate and SA regimes. For Mie-spheres, their ω increases with increasing size. SAs have higher ω values than freshly emitted aggregates (D_f = 1.8) and slightly lower and higher values than aged aggregates ($D_f \approx 3$) for monomer numbers 400–700 and >700, respectively. Alternatively, SAs have higher g values than both aggregates and Mie-spheres. The g values for aggregates increase monotonically and reach a maximum value at $D_f \approx 2.75$, after which they start to slowly decline to settle at a lower value for D_f = 3.0. Mie-spheres show even lower g values than D_f = 1.8 aggregates. This behavior can be attributed to an increase in backscattering by particles as they approach near-spherical morphology[44].

Using these calculated single-particle optical properties, we estimated the top of the atmosphere direct forcing efficiency (DFE; the radiative forcing per unit optical depth and bandwidth[45]) at 550 nm for aggregates, SAs, and Mie-spheres as functions of D_f and size (Fig. 7c). We chose the complex refractive index of soot to be 1.95–0.79i and the up-scatter fraction as a function of g per past recommendations[46,47]. The difference in the DFE value between freshly emitted (i.e. D_f = 1.8)[11] aggregates and SAs is up to +7 Wm^{-2}. This positive difference in forcing is the excessive shortwave heating of an optically thin layer of the troposphere by freshly emitted cluster-dilute aggregates compared to SAs. The forcing difference between SAs and atmospherically processed or aged aggregates (D_f = 2.5–2.7)[11,12] is negligible. However, in comparison with completely collapsed[48] ($D_f \approx 3.0$) aggregates, SAs contribute to an enhanced warming effect by ≈25% (+4 Wm^{-2}). Note that a $D_f \approx 3.0$ aggregate shouldn't be confused with a volume-equivalent Mie sphere, as simulated in climate models. The morphology of a D_f = 3.0 aggregate differs from a volume-equivalent sphere. A sphere

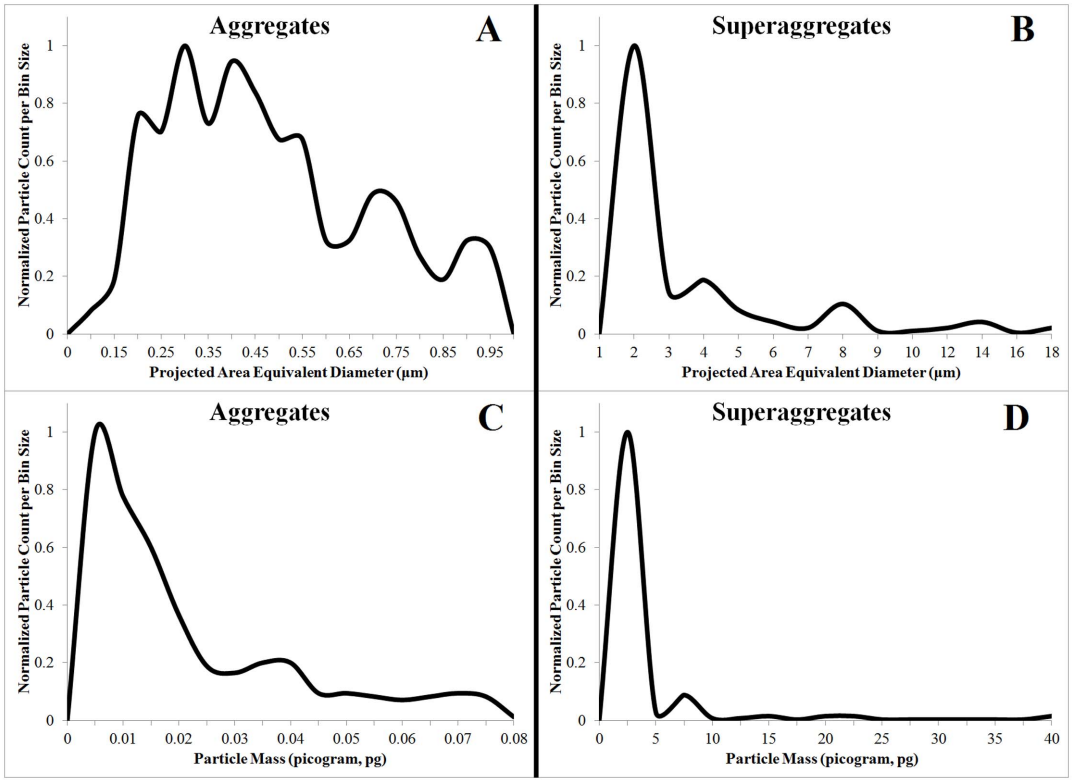

Figure 5 | Number distribution of soot aggregates and superaggregates observed during CARES. The projected area equivalent diameter number distribution (A, B) and mass distribution (C, D) of soot particles emitted from forest fires in the Sierra Nevada Foothills and the San Joaquin County regions of California, USA. The plumes were sampled in the month of June in an urban location (Sacramento), and also included inorganic aerosols in pure and externally-mixed states. These particles were not included in this statistical analysis.

has a smooth annular region compared to a $D_f = 3.0$ aggregate, which has an irregular boundary composed of monomers with voids in between them. This difference in morphology significantly affects their optical properties[49]. Our calculations show that SAs contribute 90% more warming compared to volume-equivalent Mie-spheres.

Future research direction. Taking into account both the abundance of soot SAs in the atmosphere and their microphysical properties, our findings bring to the forefront the significant impacts of these previously unrecognized pollutants on climate, human health, air pollution monitoring, and mitigation strategies. The higher heating effect of these particles, compared to volume-equivalent spheres, could change current estimates of climate forcing by models. Observation of these particles also demands new investigations on multiple research fronts. Instrument development for real-time detection and measurement of soot SAs using different size conventions, such as mobility, aerodynamic, and volume-equivalent diameters, is needed. The widely used particle-size monitoring instrument, the scanning mobility particle spectrometer[4,14], is incapable of detecting these particles. The effect of humidity and atmospheric processing on soot SAs is currently unknown. Both parameters have been shown to affect radiative properties of particles[11]. Based on future research findings, effective measures—such as appropriate mechanical filtration systems—could be employed during large-scale wildfires to help control and mitigate public health impacts of soot SAs.

Figure 6 | Schematic (*drawn using Adobe Photoshop™*) hypothesizing the soot superaggregate formation mechanism in wildfires. Particle residence times are enhanced for cluster-dilute aggregates that get trapped into one of the many vortices inside a large-scale, turbulent flame. This facilitates increase in particle volume fractions and percolation of aggregates into superaggregates inside the flame.

Methods

Aerosol sampling. In the Maldives, air was sampled from inlets on a 15 m tall tower equipped with various sensors. Aerosol particles were collected using a three-stage aerodynamic impactor (MPS-3; California Measurements, Inc.) for single-particle SEM analysis. The nominal D_a ranges for the three stages were >2, 2–0.3, and <0.3 μm. Sampling duration ranged from 45 minutes to two hours twice a day, during morning and afternoon. Particles were deposited directly onto 10 μm thick nuclepore clear polycarbonate filters (100-nm diameter pores) applied to metal stubs and located at each impactor stage[31]. Aerosol sampling during the CARES, MILAGRO, and the Las Conchas wildfire were also conducted on similar nuclepore filters using a filtration technique. After exposure, the filters were stored in a dark refrigeration unit to avoid particle transformation due to aging. Sampling duration for the CARES study was from 2331 (06/21/2010) to 0601 hours (06/22/2010) local time, while the sampling duration for the MILAGRO study was conducted from 1359 to 1546 hours on 03/28/2006. The Las Conchas fire plumes were sampled at Los Alamos between 1300 and 1800 hours on 07/22/2011.

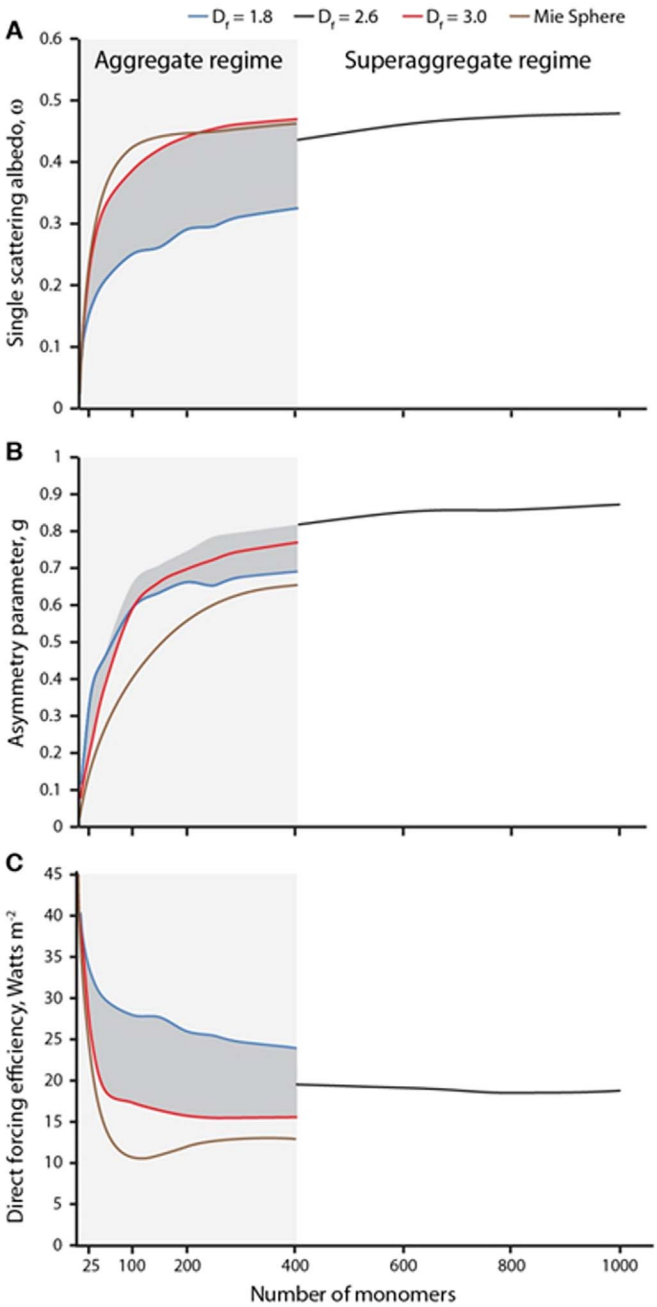

Figure 7 | Radiative properties of soot superaggregates and comparison with aggregates and spherical particles. Optical properties–single scattering albedo (A) and asymmetry parameter (B)–and direct forcing efficiency (C) dependence of aggregates and superaggregates as functions of size (number of monomers) and fractal dimension D_f. Shaded regions represent the upper and lower bound values for D_f in the range between 1.8 and 3.0. The calculations used mean refractive index = 1.95–0.79i, monomer diameter = 50 nm, and wavelength = 550 nm. Monomer number = 400 corresponds to mobility diameter = 1 μm.

Microscopy analysis. The filter samples were prepared for SEM analysis by coating them with a 1-nm thick layer of platinum to prevent aerosol charging during SEM analysis. A field-emission SEM (Hitachi S-4700) was used to analyze the coated filters for individual particle morphology and EDX analysis. A relatively moderate accelerating voltage of 20 kV was used for imaging most particles. Past studies have shown that imaging at this operating voltage has negligible impact on aggregate shape due to charging[5,33]. Images of individual particles were selected, based on the random distribution of particles on the SEM filter, for shape and size quantification.

The perimeter fractal analysis method. Calculating single-particle fractal dimension with the Perimeter Method is done by drawing grids of differing box sizes upon a 2-d image of a fractal aggregate. Given a grid with a certain box size, the number of grid boxes through which the perimeter passes is counted. A grid with a different box size is then drawn, and the number of grid boxes through which the perimeter passes is counted once again. This process is repeated, and the logarithm of the box size plotted against the logarithm of the box count, providing the parameter fractal dimension D_p as the slope. Past experimental and simulation studies[31,50,51] have confirmed the D_p of a superaggregate to be well defined and related to its mass fractal dimension D_f using the following empirical relationship:

$$D_p = 1 + \left(3 - D_f\right)^{3/2},\ D_f \geq 2, \tag{1}$$

$$D_p = D_f,\ D_f < 2. \tag{2}$$

The ensemble fractal analysis method. This method is the most accurate method for calculating D_f of an aggregate. Calculating aggregate D_f with this method involves using the relationship expressed by Equation 3 below and determining the values for the number of monomers N with the knowledge of the projected area of the aggregate (A_a), the mean projected area of the monomers (A_p), prefactor k_0 (typically approximated by a value ≈ 1), and α = 1.09

$$N = k_0 \left(\frac{A_a}{A_p}\right)^{\alpha} \tag{3}$$

Aggregate generation and T-matrix calculation. The aggregate simulation method involved generating a 3-d fractal aggregate by the particle-cluster aggregation technique[52] with a sequential algorithm that intrinsically satisfies the fundamental fractal equation[53]. For pre-specified values of D_f and prefactor (typically between 1.1 and 1.3)[54], the aggregate generation process is initiated by randomly attaching two monomers to each other, followed by the controlled addition of further monomers to the cluster at specific positions fulfilling the following conditions:1) the monomers do not intersect, i.e., they make point contact, and 2) the radius of gyration of the new aggregate (calculated based on the known positions of the monomers) satisfies the fundamental fractal equation for the fractal dimension and pre-factor selected. In this study, the pre-factor was set at 1.18 for all fractals as recommended by Oh and Sorensen[54], and the monomer diameter was set to 50 nm for all calculations, based on electron microscopy observation of superaggregates in this study. We calculate the optical properties of fractal-like soot aggregates using the efficient superposition T-matrix code developed for multi-sphere groups with random orientation. The code is documented[55] and is available on the Web, free of charge[56]. The critical advantages of this method are that it is numerically exact and is much more efficient than any other numerical technique based on an explicit solution of the Maxwell equations.

Aerosol direct forcing efficiency calculation. The shortwave aerosol DFE at the top of the atmosphere caused by a uniform, optically thin aerosol layer in the lower troposphere was calculated using

$$\frac{\Delta F}{\tau} = SD\left(1 - A_{cld}\right)T_{atm}^2\left(1 - R_{sfc}\right)^2\left[2R_{sfc}\frac{1-\omega}{\left(1-R_{sfc}\right)^2} - \beta\omega\right] \tag{4}$$

where ΔF is the change in net solar flux at the top of the atmosphere due to the presence of the aerosols, τ is the aerosol optical depth, S is the solar constant, set to 1370 Wm^{-2}, D is the fractional day length, set to 0.5, A_{cld} is the fractional cloud cover, set to 0.6, T_{atm} is the solar atmospheric transmittance, set to 0.76, R_{sfc} is the surface albedo, set to 0.15 (appropriate for an urban area), and ω is the aerosol single scattering albedo. The parameter β is the up-scatter fraction, which is a function of asymmetry parameter g as follows:

$$\beta = 0.50 - 0.45g + 0.25g^2 - 0.29g^3 \tag{5}$$

In all of the calculations, the relative humidity is assumed to be 0%.

1. Lamarque, J.-F. *et al.* Historical (1850–2000) gridded anthropogenic and biomass burning emissions of reactive gases and aerosols: methodology and application. *Atmos. Chem. Phys.* **10**, 7017–7039 (2010).
2. Bond, T. *et al.* Bounding the role of black carbon in the climate system: a scientific assessment. *J. Geophys. Res.* **118**, 5380–5552 (2013).
3. Ichoku, C., Kahn, R. & Chin, M. Satellite contributions to the quantitative characterization of biomass burning for climate modeling. *Atmos. Res.* **111**, 1–28 (2012).
4. Reid, J., Koppmann, R., Eck, T. & Eleuterio, D. A review of biomass burning emissions part II: intensive physical properties of biomass burning particles. *Atmos. Chem. Phys* **5**, 799–825 (2005).
5. Chakrabarty, R. K. *et al.* Emissions from the laboratory combustion of wildland fuels: Particle morphology and size. *J. Geophys. Res* **111**, D07204 (2006).

6. Levin, E. *et al.* Biomass burning smoke aerosol properties measured during Fire Laboratory at Missoula Experiments (FLAME). *J. Geophys. Res.* **115**, D18210 (2010).
7. McMeeking, G. R. *et al.* Emissions of trace gases and aerosols during the open combustion of biomass in the laboratory. *J. Geophys. Res.* **114**, D19210 (2009).
8. Chakrabarty, R. K. *et al.* Low fractal dimension cluster-dilute soot aggregates from a premixed flame. *Phys. Rev. Lett.* **102**, 235504 (2009).
9. Sorensen, C. & Chakrabarti, A. The sol to gel transition in irreversible particulate systems. *Soft Matter* **7**, 2284–2296 (2011).
10. Kleinstreuer, C. & Zhang, Z. Airflow and particle transport in the human respiratory system. *Annu. Rev. Fluid Mech.* **42**, 301–334 (2010).
11. Zhang, R. *et al.* Variability in morphology, hygroscopicity, and optical properties of soot aerosols during atmospheric processing. *Proc. Natl. Acad. Sci. U. S. A.* **105**, 10291–10296 (2008).
12. Kahnert, M., Nousiainen, T., Lindqvist, H. & Ebert, M. Optical properties of light absorbing carbon aggregates mixed with sulfate: assessment of different model geometries for climate forcing calculations. *Optics Express* **20**, 10042–10058 (2012).
13. Cappa, C. D. *et al.* Radiative Absorption Enhancements Due to the Mixing State of Atmospheric Black Carbon. *Science* **337**, 1078–1081 (2012).
14. Chakrabarty, R. K. *et al.* Light scattering and absorption by fractal-like carbonaceous chain aggregates: Comparison of theories and experiment. *Appl. Opt.* **46**, 6990–7006 (2007).
15. Abel, S. J., Haywood, J. M., Highwood, E. J., Li, J. & Buseck, P. R. Evolution of biomass burning aerosol properties from an agricultural fire in southern Africa. *Geophys. Res. Lett.* **30**, 1783 (2003).
16. Pósfai, M., Anderson, J. R., Buseck, P. R. & Sievering, H. Soot and sulfate aerosol particles in the remote marine troposphere. *J. Geophys. Res.* **104**, 21685–21693 (1999).
17. Martins, J. V., Hobbs, P. V., Weiss, R. E. & Artaxo, P. Sphericity and morphology of smoke particles from biomass burning in Brazil. *J. Geophys. Res.* **103**, 32051–32057 (1998).
18. Li, J., Pósfai, M., Hobbs, P. V. & Buseck, P. R. Individual aerosol particles from biomass burning in southern Africa: 2, Compositions and aging of inorganic particles. *J. Geophys. Res.* **108**, 8484 (2003).
19. China, S., Mazzoleni, C., Gorkowski, K., Aiken, A. C. & Dubey, M. K. Morphology and mixing state of individual freshly emitted wildfire carbonaceous particles. *Nat. Comm.* **4** (2013).
20. Adachi, K. & Buseck, P. R. Atmospheric tar balls from biomass burning in Mexico. *J. Geophys. Res.* **116**, D05204 (2011).
21. Lack, D. A. *et al.* Brown carbon and internal mixing in biomass burning particles. *Proc. Natl. Acad. Sci. U. S. A.* **109**, 14802–14807 (2012).
22. Pósfai, M., Simonics, R., Li, J., Hobbs, P. V. & Buseck, P. R. Individual aerosol particles from biomass burning in southern Africa: 1. Compositions and size distributions of carbonaceous particles. *J. Geophys. Res.* **108**, 8483 (2003).
23. Yokelson, R. *et al.* Emissions from biomass burning in the Yucatan. *Atmos. Chem. Phys.* **9**, 5785–5812 (2009).
24. Hoover, J. in *"Forest fire in Karnataka's tiger reserves" published in Cable News Network (IBN) news website on 03/01/2012* (Available online at: http://ibnlive.in.com/news/forest-fire-in-karnatakas-tiger-reserves/234858-3.html Retrieved 03/18/2014).
25. Ramanathan, V. *et al.* Warming trends in Asia amplified by brown cloud solar absorption. *Nature* **448**, 575–578 (2007).
26. Mazzoleni, L. R., Zielinska, B. & Moosmüller, H. Emissions of levoglucosan, methoxy phenols, and organic acids from prescribed burns, laboratory combustion of wildland fuels, and residential wood combustion. *Environ. Sci. Technol.* **41**, 2115–2122 (2007).
27. Zaveri, R. A. *et al.* Overview of the 2010 carbonaceous aerosols and radiative effects study (CARES). *Atmos. Chem. Phys.* **12**, 7647–7687 (2012).
28. Aiken, A. *et al.* Mexico City aerosol analysis during MILAGRO using high resolution aerosol mass spectrometry at the urban supersite (T0)–Part 1: Fine particle composition and organic source apportionment. *Atmos. Chem. Phys.* **9**, 6633–6653 (2009).
29. DeCarlo, P. *et al.* Fast airborne aerosol size and chemistry measurements above Mexico City and Central Mexico during the MILAGRO campaign. *Atmos. Chem. Phys.* **8**, 4027–4048 (2008).
30. Chakrabarty, R. K. *et al.* Simulation of Aggregates with Point-Contacting Monomers in the Cluster–Dilute Regime. Part 1: Determining the Most Reliable Technique for Obtaining Three-Dimensional Fractal Dimension from Two-Dimensional Images. *Aerosol Sci. Technol.* **45**, 75–80 (2011).
31. Chakrabarty, R. K., Moosmuller, H., Garro, M. A. & Stipe, C. B. Observation of Superaggregates from a Reversed Gravity Low-Sooting Flame. *Aerosol Sci. Technol.* **46**, I–Iii, doi:Doi 10.1080/02786826.2011.608389 (2012).
32. Kearney, S. P. & Pierce, F. Evidence of soot superaggregates in a turbulent pool fire. *Combust. Flame* **159**, 3191–3198 (2012).
33. Chakrabarty, R. K. *et al.* Light Scattering and Absorption by Fractal-Like Carbonaceous Chain Aggregates: Comparison of Theories and Experiment. *Appl. Opt.* **46**, 6990–7006 (2007).
34. Stipe, C. B., Higgins, B. S., Lucas, D., Koshland, C. P. & Sawyer, R. F. Inverted co-flow diffusion flame for producing soot. *Rev. Sci. Instrum.* **76**, 023908 (2005).
35. Kim, W., Sorensen, C. & Chakrabarti, A. Universal occurrence of soot superaggregates with a fractal dimension of 2.6 in heavily sooting laminar diffusion flames. *Langmuir* **20**, 3969–3973 (2004).
36. Chakrabarty, R. *et al.* Brown carbon in tar balls from smoldering biomass combustion. *Atmos. Chem. Phys* **10**, 6363–6370 (2010).
37. Pósfai, M. *et al.* Atmospheric tar balls: Particles from biomass and biofuel burning. *J. Geophys. Res.* **109** (2004).
38. Slowik, J. G. *et al.* Particle morphology and density characterization by combined mobility and aerodynamic diameter measurements. Part 2: Application to combustion-generated soot aerosols as a function of fuel equivalence ratio. *Aerosol Sci. Technol.* **38**, 1206–1222 (2004).
39. Andreae, M. O. & Ramanathan, V. Climate's dark forcings. *Science* **340**, 280–281 (2013).
40. Heyder, J., Gebhart, J., Rudolf, G., Schiller, C. F. & Stahlhofen, W. Deposition of particles in the human respiratory tract in the size range 0.005–15 μm. *J. Aerosol Sci.* **17**, 811–825 (1986).
41. Dhaubhadel, R., Gerving, C. S., Chakrabarti, A. & Sorensen, C. M. Aerosol gelation: Synthesis of a novel, lightweight, high specific surface area material. *Aerosol Sci. Technol.* **41**, 804–810 (2007).
42. Vilela, R. D. & Motter, A. E. Can aerosols be trapped in open flows? *Phys. Rev. Lett.* **99**, 264101 (2007).
43. Liu, L. & Mishchenko, M. I. Scattering and radiative properties of complex soot and soot-containing aggregate particles. *J. Quant. Spectrosc. Radiat. Transfer* **106**, 262–273 (2007).
44. Mishchenko, M. I., Travis, L. D. & Lacis, A. A. *Scattering, absorption, and emission of light by small particles*. (Cambridge university press, 2002).
45. Chylek, P. & Wong, J. Effect of absorbing aerosols on global radiation budget. *Geophys. Res. Lett.* **22**, 929–931 (1995).
46. Bond, T. C. & Bergstrom, R. W. Light absorption by carbonaceous particles: An investigative review. *Aerosol Sci. Technol.* **40**, 27–67 (2006).
47. Wiscombe, W. & Grams, G. The backscattered fraction in two-stream approximations. *J. Atmos. Sci.* **33**, 2240–2451 (1976).
48. Lewis, K. *et al.* Reduction in biomass burning aerosol light absorption upon humidification: roles of inorganically-induced hygroscopicity, particle collapse, and photoacoustic heat and mass transfer. *Atmos. Chem. Phys* **9**, 8949–8966 (2009).
49. Liu, L., Mishchenko, M. I. & Patrick Arnott, W. A study of radiative properties of fractal soot aggregates using the superposition *T*-matrix method. *J. Quant. Spectrosc. Radiat. Transfer* **109**, 2656–2663 (2008).
50. Jullien, R., Kolb, M. & Botet, R. Diffusion limited aggregation with directed and anisotropic diffusion. *J. de Phys.* **45**, 395–399 (1984).
51. Dhaubhadel, R., Pierce, F., Chakrabarti, A. & Sorensen, C. Hybrid superaggregate morphology as a result of aggregation in a cluster-dense aerosol. *Phys. Rev. E* **73**, 011404 (2006).
52. Chakrabarty, R., Garro, M., Chancellor, C., Herald, C. & Moosmüller, H. FracMAP: A Graphical User-Interactive Package for Performing Simulation and Morphological Analysis of Fractal-Like Aerosol Agglomerates. *Comput. Phys. Commun* **180**, 1376–1381 (2009).
53. Sorensen, C. M. Light scattering by fractal aggregates: A review. *Aerosol Sci. Technol.* **35**, 648–687 (2001).
54. Oh, C. & Sorensen, C. M. The Effect of Overlap between Monomers on the Determination of Fractal Cluster Morphology. *J. Colloid Interface Sci.* **193**, 17–25 (1997).
55. Mackowski, D. W. & Mishchenko, M. I. Calculation of the T-matrix and the scattering matrix for ensembles of spheres. *JOSA A* **13**, 2266–2278 (1996).
56. Mackowski, D., Fuller, K. & Mishchenko, M. *Codes for Calculation of Scattering by Clusters of Spheres* (Available at: ftp://ftp.eng.auburn.edu/pub/dmckwski/scatcodes/index.html), Retrieved 03/18/2014).
57. Haagenson, G. in *"Fire on shore of Millerton Lake contained" published in American Broadcasting Company (ABC30) news website on 06/22/2010* (Available online at: http://abclocal.go.com/kfsn/story?section=news/local&id=7515202 Retrieved 03/18/2014).

Acknowledgments

This material is based upon work supported by NASA (NNX10AR89A, NNX11AB79G and NNX12AN97H), the U.S. Department of Energy Atmospheric System Research (DE-SC0010019 and F265-LANL(PI-MKD)), the U.S. National Science Foundation Division of Atmospheric and Geospace Sciences (ATM07-21142), and the Desert Research Institute. We thank V. Ramanathan for facilitating our participation in the field campaign at Maldives; K. Gorkowski for his help with sampling aerosols during CARES and the Las Conchas fire; Ö. Gustafsson for providing quartz fiber filter samples; B. Zielinska and her laboratory for performing mass spectrometry analyses of quartz fiber filters; M. Ahmadian for assisting with microscopy analysis; L. Wable for illustrations; R. Kreidberg for help with editing the manuscript; and C.M. Sorensen for insightful discussions.

Author contributions

R.K.C. conceived and led the study, including project coordination and manuscript preparation; N.D.B., S.C., C.M. and M.K.D. were involved with particle sampling and data collection; N.D.B. and S.C. performed the SEM analysis; R.K.C., N.D.B. and S.C. were involved with data analysis; R.K.C., N.D.B., H.M., L.L. and M.I.M. performed optical

modeling and radiative forcing calculations. All authors discussed the results and contributed to the manuscript.

Additional information

Supplementary information accompanies this paper at http://www.nature.com/scientificreports

Competing financial interests: The authors declare no competing financial interests.

How to cite this article: Chakrabarty, R.K. *et al.* Soot superaggregates from flaming wildfires and their direct radiative forcing. *Sci. Rep.* **4**, 5508; DOI:10.1038/srep05508 (2014).

This work is licensed under a Creative Commons Attribution-NonCommercial-ShareAlike 4.0 International License. The images or other third party material in this article are included in the article's Creative Commons license, unless indicated otherwise in the credit line; if the material is not included under the Creative Commons license, users will need to obtain permission from the license holder in order to reproduce the material. To view a copy of this license, visit http://creativecommons.org/licenses/by-nc-sa/4.0/

SCIENTIFIC REPORTS

OPEN

Corrigendum: Soot superaggregates from flaming wildfires and their direct radiative forcing

Rajan K. Chakrabarty, Nicholas D. Beres, Hans Moosmüller, Swarup China, Claudio Mazzoleni, Manvendra K. Dubey, Li Liu & Michael I. Mishchenko

Scientific Reports 4:5508; doi: 10.1038/srep05508; published online 01 July 2014; updated on 10 March 2016

The original version of this Article contained an error in the Abstract.

"We estimate that SAs contribute, per unit optical depth, up to 35% less atmospheric warming than freshly-emitted ($D_f \approx 1.8$) aggregates, and ≈90% more warming than the volume-equivalent spherical soot particles simulated in climate models."

now reads:

"At 550 nm wavelength, we estimate that SAs contribute, per unit optical depth, up to 35% less atmospheric warming than freshly-emitted ($D_f \approx 1.8$) aggregates, and ≈90% more warming than the volume-equivalent spherical soot particles simulated in climate models."

Additionally, the original version of this Article contained an error in the Methods section.

"The parameter β is the up-scatter fraction, which is a function of asymmetry parameter g as follows:"

now reads:

"The parameter β is the up-scatter fraction, which is a function of asymmetry parameter g using the Henyey-Greenstein phase function as follows:"

These errors have been corrected in the HTML version of the Article but have not been corrected in the PDF version of the Article.

This work is licensed under a Creative Commons Attribution-NonCommercial- ShareAlike 4.0 International License.The images or other third party material in this article are included in the article's Creative Commons license, unless indicated otherwise in the credit line; if the material is not included under the Creative Commons license, users will need to obtain permission from the license holder in order to reproduce the material. To view a copy of this license, visit http://creativecommons.org/licenses/by-nc-sa/4.0/